

Myelin water fraction mapping from multiple echo spin echoes and an independent B_1^+ map

Nima Mehdizadeh  | Alan H. Wilman

Department of Biomedical Engineering,
University of Alberta, Edmonton, Alberta
Canada

Correspondence

Nima Mehdizadeh, Department of
Biomedical Engineering, University of
Alberta, 1098 Research Transition Facility,
Edmonton, Alberta, T6G 2V2, Canada.
Email: nmehdiza@ualberta.ca

Funding information

Canadian Institutes of Health Research,
Grant/Award Number: PS 180473;
Natural Sciences and Engineering
Research Council of Canada, Grant/Award
Number: RGPIN-2017-04006

Purpose: Myelin water fraction (MWF) is often obtained from a multiple echo spin echo (MESE) sequence using multi-component T_2 fitting with non-negative least squares. This process fits many unknowns including B_1^+ to produce a T_2 spectrum for each voxel. Presented is an alternative using a rapid B_1^+ mapping sequence to supply B_1^+ for the MWF fitting procedure.

Methods: Effects of B_1^+ errors on MWF calculations were modeled for 2D and 3D MESE using Bloch and extended phase graph simulations, respectively. Variations in SNR and relative refocusing widths were tested. Human brain experiments at 3 T used 2D MESE and an independent B_1^+ map. MWF maps were produced with the standard approach and with the use of the independent B_1^+ map. Differences in B_1^+ and mean MWF in specific brain regions were compared.

Results: For 2D MESE, MWF with the standard method was strongly affected by B_1^+ misestimations arising from limited SNR and response asymmetry around 180° , which decreased with increasing relative refocusing width. Using an independent B_1^+ map increased mean MWF and decreased coefficient of variation. Notable differences in vivo in 2D MESE were in areas of high B_1^+ such as thalamus and splenium where mean MWF increased by 88% and 31%, respectively ($P < 0.001$). Simulations also demonstrated the advantages of this approach for 3D MESE when SNR is < 500 .

Conclusion: For 2D MESE, because of increased complexity of decay curves and limited SNR, supplying B_1^+ improves MWF results in peripheral and central brain regions where flip angles differ substantially from 180° .

KEYWORDS

flip angle estimation, multi-component T_2 fitting, myelin water fraction, stimulated echoes

1 | INTRODUCTION

Transverse relaxation (T_2) mapping is commonly performed with a multiple echo spin echo (MESE) technique,

though other methods are possible. As shown by MacKay,¹ multiple component analysis of the transverse decay in in vivo brain can yield the myelin water fraction (MWF), identified as the proportion of the short T_2 component in

This is an open access article under the terms of the Creative Commons Attribution-NonCommercial License, which permits use, distribution and reproduction in any medium, provided the original work is properly cited and is not used for commercial purposes.

© 2022 The Authors. *Magnetic Resonance in Medicine* published by Wiley Periodicals LLC on behalf of International Society for Magnetic Resonance in Medicine.

the voxel. Use of this method is widespread and has particular application to multiple sclerosis, a demyelinating disease.¹⁻⁷ Spectrum analysis of the T_2 decay data provides underlying water compartments, including myelin water and intra-/extracellular water.^{1,5,7-11} The MWF increases the specificity of T_2 mapping to myelin, although other short T_2 species may serve as a confound.^{12,13}

Perfect 180° refocusing in MESE sequences is required to generate an exclusively T_2 modulated signal decay. In practice, the theoretical refocusing stipulation is violated because of: imperfect refocusing profiles, transmit calibration errors, and radio frequency (RF) interference effects,¹⁴ which all collude to alter the range of refocusing angles across the volume of interest.¹⁵ Hence, mono- or multi-exponential fittings of the corresponding T_2 times need to account for such effects.¹⁵⁻¹⁷

Recent literature for MWF estimation from a MESE sequence includes stimulated echo compensation and uses a multi-exponential fit with a regularized non-negative least squares (NNLS) algorithm to decompose decay curves into T_2 distributions with no prior assumption about the number of contributing T_2 components.^{5,16,18,20,21} However, the fitting requires knowledge of the transmit RF field (B_1^+) in each voxel that modulates the nominal angles prescribed. Therefore, to produce proper dictionary matrices for the NNLS process, it is common practice to perform a B_1^+ optimization step to estimate the apparent B_1^+ of the decay curve.^{11,16,18-22} However, estimation of the B_1^+ parameter from the echo train is complicated by oscillating behavior of stimulated echoes and noise and could lead to increased susceptibility of NNLS fit results to noise.^{19-21,23}

Modeling of the MESE signal decay may be performed in many ways including using the extended phase graph (EPG) algorithm,^{24,25} which computes multi-echo signal decay curves given T_1 , T_2 , inter-echo spacing time, and the corresponding refocusing angle. This EPG method is used in current regularized NNLS fitting algorithms designed particularly for 3D MESE experiments that can be modeled by a single flip angle in each voxel and have symmetry around a refocusing angle of 180° .^{16,18-21} However, for slice selective RF pulses, the analysis is more complex, requiring accounting for RF slice profile effects.^{11,15,22} Particularly for 2D slice selective MESE sequences, Bloch modeling is needed to exactly account for RF pulse profile effects across the voxel. For example, recent work using single component T_2 fitting of a 2D MESE sequence demonstrated different fitting results for B_1^+ and T_2 depending on how the RF pulses were simulated.²⁶ In particular, flip angle errors were substantial when estimating the flip angle from the decay curve train using EPG methods without Bloch modeling of the RF profiles. Furthermore, even when using Bloch modeling, the flip angle estimate was

not in exact agreement with the measured angle, because of multiple possible similar solutions and the presence of noise. Akhondi-Asl and colleagues²² have recently demonstrated MWF mapping from 2D MESE using full Bloch modeling to more precisely model the signal decay. However, this method still estimates the B_1^+ from the 2D MESE echo train to obtain the apparent B_1^+ value and any B_1^+ misestimations may affect the MWF estimation.

Here, we investigated whether supplying the B_1^+ values to the fitting process, via an independent B_1^+ map, would increase the precision of MWF estimations compared to the standard approach of using the apparent B_1^+ via an optimization step derived from the MESE echo train. This new approach for MWF estimation eliminates the extra B_1^+ optimization step, but requires a B_1^+ map that has proven successful for single component T_2 mapping.²⁶ We investigated the value of this approach for MWF estimation in simulations of 2D and 3D MESE sequences and in vivo human brain experiments with 2D MESE.

2 | METHODS

2.1 | Simulation of T_2 decay data

Visible water compartments in the brain water pool can be categorized into 3 environments: myelin water (MW), intra-extra cellular water (IEW), and cerebrospinal fluid.^{1,7-10} We defined a model for simulations, which only consists of MW ($T_2 = 15$ ms, $T_1 = 600$ ms) and IEW ($T_2 = 75$ ms, $T_1 = 1000$ ms) environments, corresponding to healthy white matter (WM).^{4,5,16,18-21,27-30}

Using this model, simulated T_2 decays were created, with an extra step to calculate Rician noise effects. Note that because the echo train decays to near 0, Rician noise was used rather than Gaussian.^{20,21,31} For simulation of 3D MESE data with nonselective refocusing pulses the EPG algorithm was used; however, for 2D MESE data generation full Bloch modeling was incorporated to account for the slice profile across the voxel.^{22,32} The T_2 distributions for each water compartment are generated using a truncated Gaussian distribution with a SD of 10% of the mean and were truncated to 0 for values farther than 2 SDs from the mean.²⁸ We defined the signal-to-noise ratio (SNR) as:

$$SNR = \frac{\max(S(t))}{\sigma} \quad (1)$$

where σ is the standard deviation of the Rician noise and $S(t)$ is the decay signal available at each time t in the echo train. Note that the maximum signal is not necessarily at the first echo due to stimulated echo contributions. All the simulations used 32 echoes and 10 ms inter-echo spacing. Sequence parameters for the 2D MESE matched in vivo

experiments. For 3D, nonselective refocusing pulses were assumed.

2.2 | Analysis and T_2 distribution process

The 3D MESE data (simulation only) were analyzed on a voxel-based approach using the regularized NNLS algorithm with stimulated echo estimation (<https://mriresearch.med.ubc.ca/news-projects/myelin-water-fraction/>). This method uses the standard model for T_2 analyses,^{16,18–21,27} which does not make any priori assumptions about the distribution of signal decay.^{16,18,21,27}

Set parameters included 60 logarithmically spaced T_2 times, and T_2 range from 8 ms to 2 s with the lower limit slightly smaller than echo-spacing to better capture the MW peak.²¹ A constant T_1 value (= 1 s) is used for all decay curves and voxels because it has been shown to have negligible error.¹⁶ The refocusing flip angle experienced by the voxel needs to be set or apparent values need to be estimated.

For 2D MESE data (simulation and in vivo data), the fitting procedure used the same regularized NNLS algorithm discussed above for 3D data; however, decay curve generation required a different approach because of the slice profile effects across each voxel. The pulse sequence train was simulated to produce decay curves from a protocol file containing exact timings, gradient, and RF field that was then fed into the Bloch simulator code project (<http://www-mrsrl.stanford.edu/~brian/blochsim/>) that provides the magnetization vector at each given time and point in space. The code used 513 equally spaced points across $3\times$ the slice-thickness. The 2D signal decay curve generation was handled using in-house wrapper code by summation of magnetizations across the slice profile at each required echo time point. The same range of T_2 values as 3D was used to generate dictionary matrices.

As per common practice, a regularization term was added for the NNLS fitting, so that there would be an $\sim 2\%$ increase in the sum of the squared residual of the fitted curve.^{5,20,21} Finally, after acquiring the solution, myelin water fraction was determined by applying a T_2 threshold of 40 ms.^{1,7,8,11,16,21}

2.3 | B_1^+ estimation

Typically, several linearly spaced B_1^+ values (for 3D, usually 8 flip angles ranging from 100° to 180°)^{16,21} are tested to enable B_1^+ estimation from NNLS solutions. Next, by back projecting the solution and comparing to the experimental decay curve, the sum of squares measure of residuals or χ^2 is computed. Finally, χ^2 values versus B_1^+ is fed

to a cubic spline function to interpolate the 8 data point curve. The assumption is that the true B_1^+ would produce the smallest χ^2 , therefore, by finding the B_1^+ that corresponds to minimum χ^2 , the B_1^+ estimate or apparent B_1^+ value is obtained to use for generating the basis decay curves for the regularized NNLS process.^{16,18–21,27} This process is usually done for 3D data, but for 2D data a similar procedure is performed with the difference that the grid search for the correct B_1^+ is done over the entire range used in the lookup table (here, we used 1401 data points ranging from 0.5–1.5 in steps of 0.001) instead of using limited data points across the range.²²

The difference in the B_1^+ estimation process for 2D and 3D MESE relates to the greater complexity of 2D MESE curves that arises from the slice profile and the resulting asymmetry of 2D MESE decay around B_1^+ value of 1 (flip angle of 180°), which add to the complexity of estimation.

2.4 | Numerical simulations

The effect of B_1^+ miscalculation was considered by varying the error in the fitted B_1^+ from -0.3 to $+0.3$ using 0.01 increments. The B_1^+ range was 0.6 to 1.4 for 2D data, whereas for 3D data, B_1^+ did not exceed 1.0 because the EPG outcome is symmetric around 1.0 (i.e., B_1^+ of 1.1 results in the same decay curve as 0.9). The fractions for water compartments were 85% IEW (mean $T_2 = 75$ ms, SD = 7.5 ms), and 15% MW (mean $T_2 = 15$ ms, SD = 1.5 ms). The procedure at each B_1^+ value was repeated 500 times (SNR of 200) with the aforementioned simulation relaxation parameters to calculate the mean of MWF estimations. The mean MWF estimation versus B_1^+ difference from ground truth was examined.

To compare the precision of the multi-component fit of the 2 approaches, the coefficient of variance (CoV%) of the MWF estimation at different SNR values ranging from 50 to 1000 in increments of 50 was calculated using the same water compartment values as above. The procedure was repeated 1000 times at each B_1^+ value (ranging from 0.7 to 1.3 using 0.05 step size).

To address the effect of different slice profiles, we simulated a range of refocusing to excitation slice-thickness ratios (relative refocusing width ranging from 1 to 4) using the standard unmodulated Hanning filtered sinc RF refocusing pulses of 2.9 ms duration. We also simulated a tailored low specific absorption rate (SAR) variable-rate selective excitation (VERSE) pulse (3.84 ms length time) with 1.2 relative refocusing width. We used the same parameters mentioned above using 500 realizations of noise to calculate CoV% of MWF estimations using the 2 methods.

2.5 | In vivo experiments

Human brain data were acquired from 5 healthy volunteers (22-42 years old) at 3 T (Prisma, Siemens Healthcare, Erlangen, Germany) using a 64-channel head coil. All subjects provided informed consent and this study was approved by the University Ethics Board. A 32 echo 2D MESE sequence was used for T_2 measurement ($TE/\Delta TE/TR = 10/10/1000$ ms, 4 slices, unmodulated Hanning-windowed sinc shaped refocusing pulses with 2.9 ms duration, refocusing/excitation slice-thickness factor 1.2, in-plane resolution 1.2×1.3 mm, slice thickness 5 mm, slice gap 200%, 3 averages, and acquisition time 12 min and 14 s). A 3D T_1 weighted MPRAGE sequence was collected for region segmentation (1 mm isotropic resolution, 3.6 min). A Bloch-Siegert flip angle mapping sequence³⁸ was used using spatial resolution $1.25 \times 1.25 \times 3.0$ mm³ and 37 s acquisition time. Images were registered using the SPM12 MATLAB toolbox (The MathWorks, Natick, MA).

Images were analyzed to produce MWF maps using the aforementioned processes. Comparisons were made between the standard approach using the apparent B_1^+ from the echo train, and the new method that uses a supplied B_1^+ map. MWF maps were compared using manually segmented regions of interest (ROI) and the scatter plots of all voxels in the central slices. Plots compared the supplied to the apparent B_1^+ values and the difference of MWF values estimated by the 2 methods. The ROIs were performed in 3 WM areas (frontal WM, genu, splenium, and forceps major) and 2 deep gray matter territories (thalamus, caudate). A student t test was used to reject the null hypothesis of equal mean MWF in each ROI. MWF differences of the 2 methods were also compared to the ground truth B_1^+ values.

3 | RESULTS

Figure 1 shows the signal responses generated from the Bloch simulation of the 2D MESE sequence using a Hanning-windowed sinc pulse (as used in in vivo experiments) (Figure 1A,C) and a low SAR VERSE pulse (Figure 1C,D). The magnitude signal response profiles and decay curves show a larger second echo owing to the recovery of stimulated echoes, despite the fact that both refocusing pulses are identical. The slice response profiles of the tailored low SAR pulse are somewhat wider. These normalized 2D MESE decay curves lack symmetry around B_1^+ of 1 as previously recognized,²⁶ although there is much similarity between them. Histograms of the flip angle and apparent B_1^+ results for 3D and 2D simulations are shown in (Figure 1E-H). For 2D MESE data

(Figure 1E,F), 2 distinct peaks are evident, with approximate symmetry around B_1^+ of 1.0 and the smaller peak shrinking as SNR increases. The 3D MESE data estimation results (Figure 1G,H) show poorer results for the larger flip angle at smaller SNR values with the probability of misestimating the flip angle to 180° rising as the SNR decreases and also when the actual flip angle gets closer to the upper boundary.

Figure 2 illustrates the effect of having a bias in the B_1^+ parameter (B_1^+ error) and the effects of SNR on MWF when using an MWF of 15% for 2D and 3D MESE. For the 3D MESE data (Figure 2A), only B_1^+ values less than 1.0 are shown because of exact symmetry around 1.0. In contrast, for 2D MESE (Figure 2B), the B_1^+ values greater than 1.0 do not generate symmetrical values, although they are similar with an opposite slope. The effect of SNR on the CoV% of the MWF estimation is shown in (Figure 2C-E). Supplying the B_1^+ values for 2D and 3D MESE data yields improvements with the 2D MESE data showing the greatest differences. Importantly, the supplied B_1^+ method performs similarly for different B_1^+ values, whereas the apparent B_1^+ method is quite dependent on this variable. Figure 2E shows the results of RF pulse alterations, demonstrating that increasing the refocusing to excitation thickness ratio in 2D MESE reduces the difference between the 2 methods. In addition, the RF pulse type affects results with the low SAR pulse showing the largest difference between methods. The general pattern of improvement is observed when supplying the B_1^+ parameter in all cases, with greatest effects in 2D MESE.

A typical example of apparent and supplied B_1^+ maps and resulting MWF is shown in Figure 3. Most of the apparent B_1^+ values are close to 1.0 with clear underestimation in central regions where the supplied map is >1.0 . The 2 methods yield similar MWF maps; however, there are local differences that are pointed out by the arrows, which are in alignment with the local misestimations in the B_1^+ maps and the difference MWF map. Generally, the local errors caused by the misestimations in the apparent B_1^+ when using the signal decay optimization step resulted in underestimated MWF values.

The in vivo ROI analysis of MWF maps in Table 1 illustrates mean MWF values are elevated when using the proposed method (except for genu of corpus callosum where there is no difference). The linear correlation between the 2 approaches was generally high; however, in regions where supplied B_1^+ values were much greater than 1.0 (splenium of corpus callosum and thalamus), the correlation coefficient is reduced (0.8 and 0.7). Other ROIs show high linear correlation values (>0.9) and the mean B_1^+ observed in these territories was close to 1.0. Generally, the CoV% (intra-subject) of mean MWF values decreases using

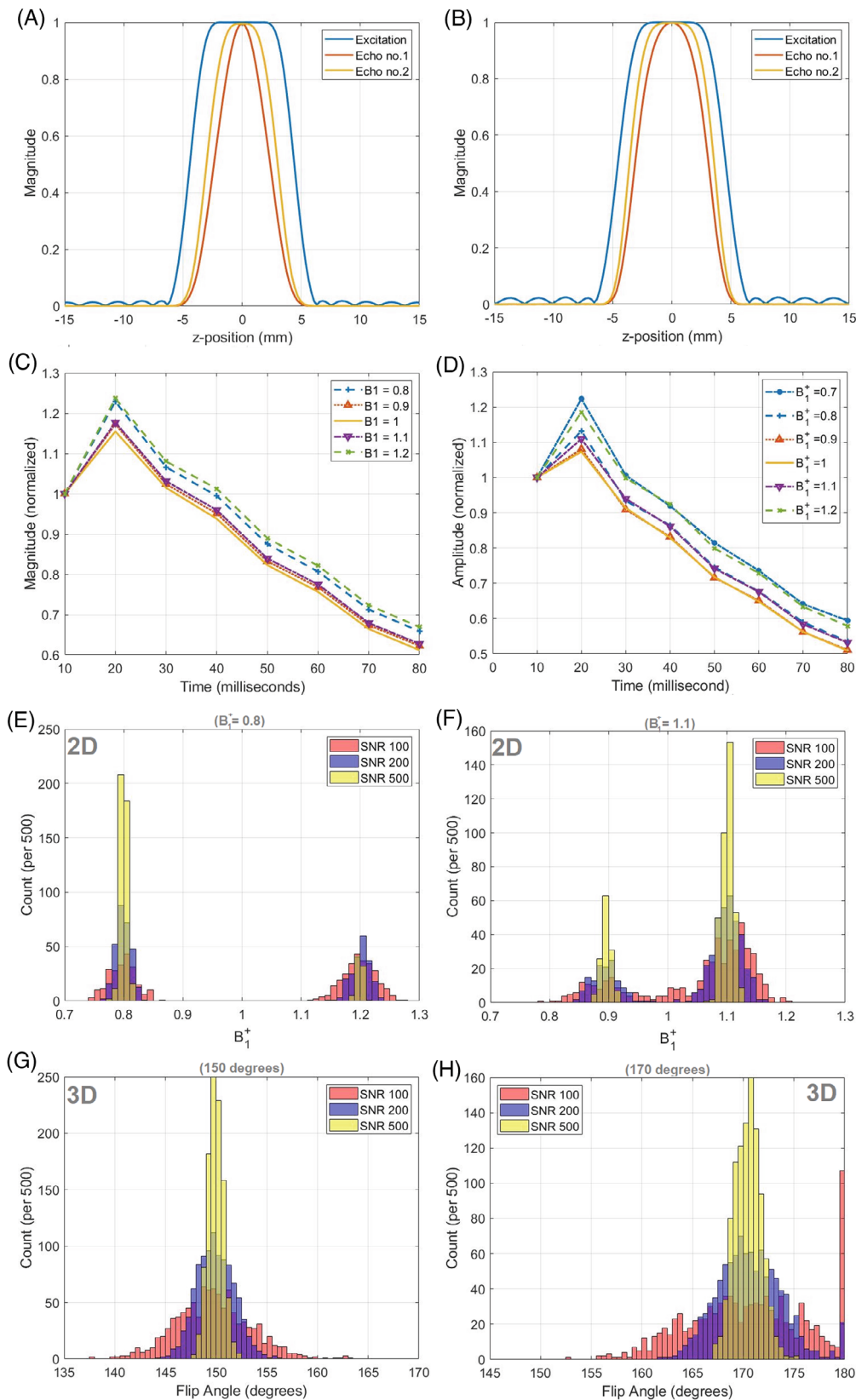


FIGURE 1 RF pulse and signal decay simulations for 2D MESE are shown along with simulated B_1^+ histograms for 2D and 3D MESE sequences. Bloch simulation results for 2D MESE used a standard Hanning-windowed sinc pulse (A,C) or a low SAR VERSE pulse (B,D) both with a refocusing to excitation thickness factor of 1.2.

Magnitude signal response across the slice profile for excitation and the first 2 echoes are shown (A,B) along with normalized 2D MESE simulated signal decay curves using T_2 of 75 ms (C,D). Note the similar decay curves for disparate B_1^+ values.

Histograms of apparent B_1^+ results from the optimization step at 3 SNR levels (100, 200, and 500) for 2D and 3D MESE simulations using MWF of 15% and standard RF parameters are shown in (E-H). Histograms for 2D MESE data are shown where the ground truth is B_1^+ of 0.8 in (E) and B_1^+ of 1.1 in (F).

3D MESE results are shown when the actual flip angle was (G) 150°, and (H) 170°. For 2D MESE, variations may occur even at SNR of 500, owing to similar solutions on either side of B_1^+ of 1.0. In contrast, 3D results are more focused owing to exact symmetry in the signal response on either side of 180° because of only a single flip angle value affecting the whole voxel

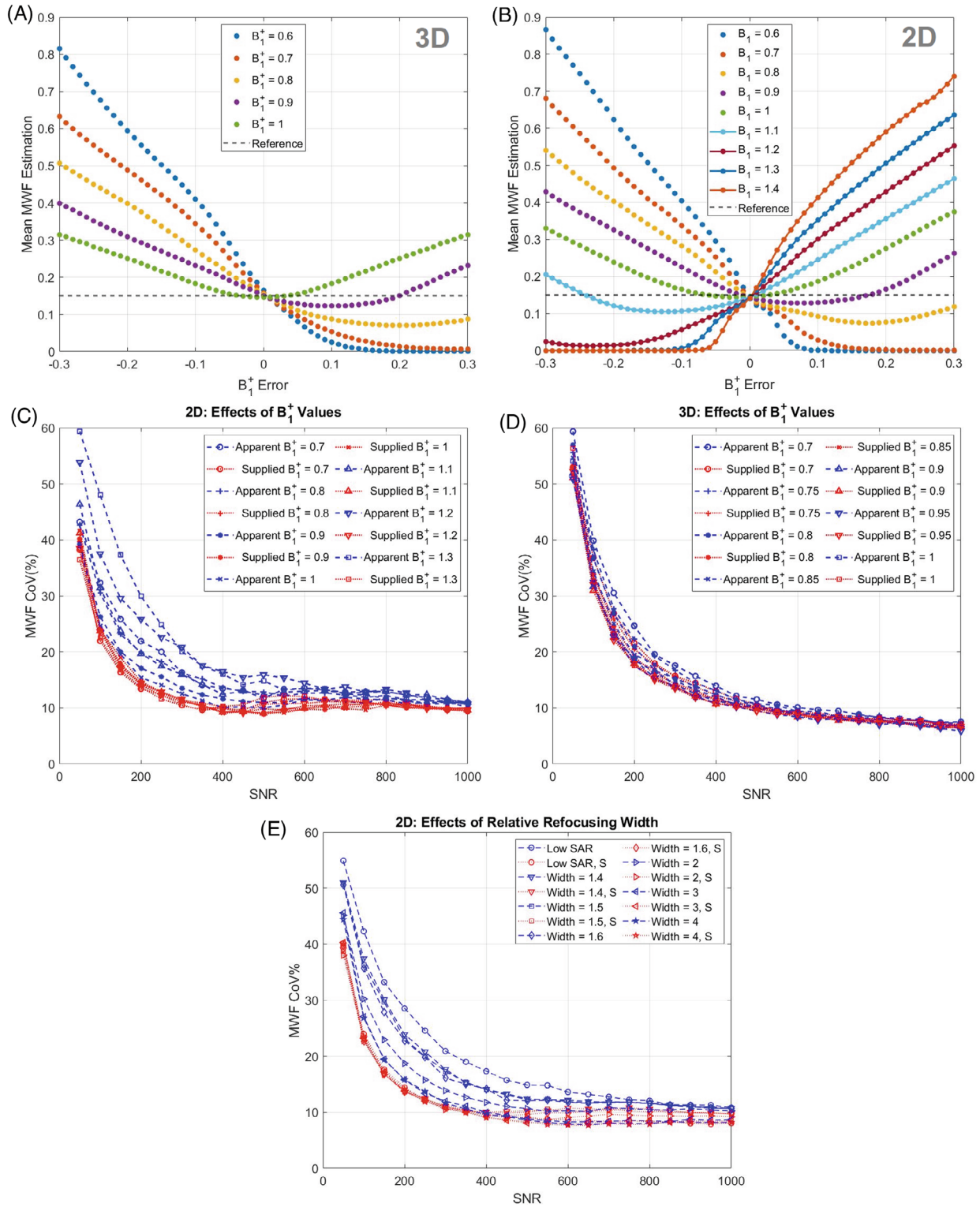


FIGURE 2 Effect of B_1^+ error (A,B) and SNR (C-E) on MWF estimations using 15% MWF. The effect of B_1^+ error on the MWF estimation is simulated with an SNR of 200 and a nominal angle of 180° using (A) 3D nonselective refocusing, and (B) 2D slice selective MESE with standard RF parameters (1.2 relative refocusing width, Hanning windowed sinc). The effect of SNR on MWF coefficient of variation (CoV%) is illustrated for a range of B_1^+ values and relative refocusing widths. (C) 2D MESE using the refocusing to excitation ratio of 1.2, (D) 3D MESE simulations with nonselective refocusing, and (E) 2D MESE using a range of refocusing to excitation ratios for the standard RF pulse and a low SAR VERSE pulse with thickness ratio of 1.2. MWF CoV% is shown in blue for the apparent B_1^+ method and red for the supplied B_1^+ . 1000 different Rician noise realizations were used in each case. For 3D MESE B_1^+ , only values <1.0 are plotted as curves are symmetrical around this value (analogous to flip angle of 180°). In (E), the letter “S” indicates the supplied B_1^+ method and a range of B_1^+ values (from 0.6 to 1.4) were used to calculate the average values at each relative refocusing width

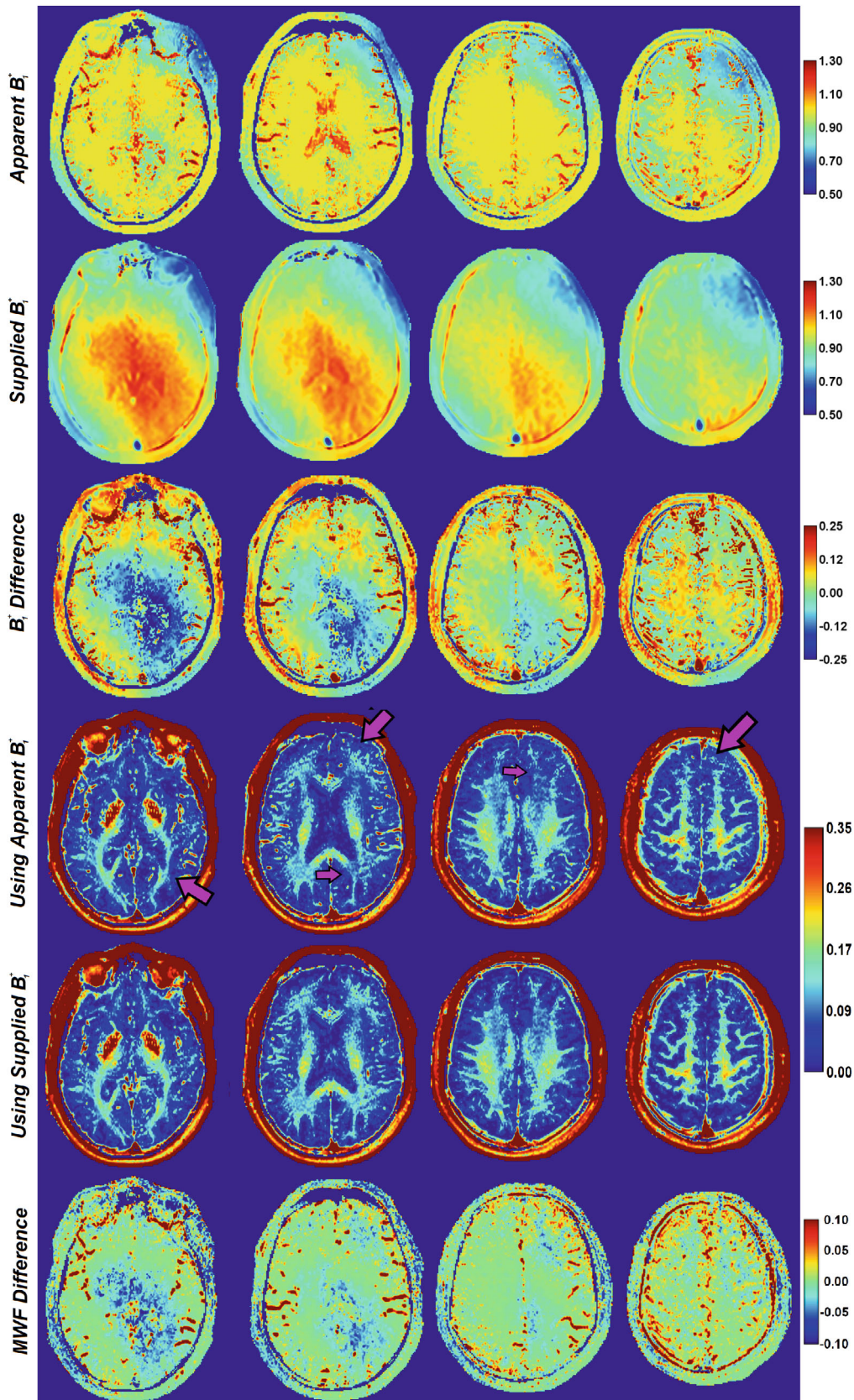


FIGURE 3 B_1^+ mapping and MWF maps from 1 subject. The apparent B_1^+ from the decay train optimization step (top row) and the supplied B_1^+ maps (second row) are shown, along with the difference image (third row). In particular, the apparent B_1^+ from the decay train underestimates high B_1^+ found in central regions and extending to the posterior periphery in this subject. MWF maps are shown using apparent B_1^+ values (fourth row), supplied B_1^+ values from the independent B_1^+ map (fifth row), and the difference map of the 2 (bottom row). Four slices from a single subject are shown. Purple arrows point to areas with visible MWF improvements when supplying the B_1^+ values

TABLE 1 Mean and standard deviation of MWF values across all subjects

Region of interest	MWF (%) from apparent B_1^+ (mean; SD)	MWF (%) from supplied B_1^+ (mean; SD)	P -value (t test)*	Correlation coefficient ^a	Supplied B_1^+ values (mean; SD)
Splenium	14.0; 3.5	18.3; 3.1	1.2×10^{-6}	0.80	1.13; 0.03
Genu	13.7; 3.7	13.7; 3.7	0.9	1.00	0.98; 0.03
Caudate	4.8; 1.8	6.2; 1.9	2.1×10^{-6}	0.91	1.05; 0.03
Thalamus	5.9; 1.2	11.1; 1.1	2.0×10^{-6}	0.70	1.15; 0.03
Frontal WM	12.3; 1.6	12.9; 1.6	5.8×10^{-6}	0.99	0.93; 0.02
Entire WM	12.2; 1.4	13.2; 1.2	1.6×10^{-6}	0.98	0.98; 0.03

^aThe linear correlation coefficient of the mean MWF between the 2 methods.

* P -values show the significance of the mean MWF difference when comparing the 2 methods.

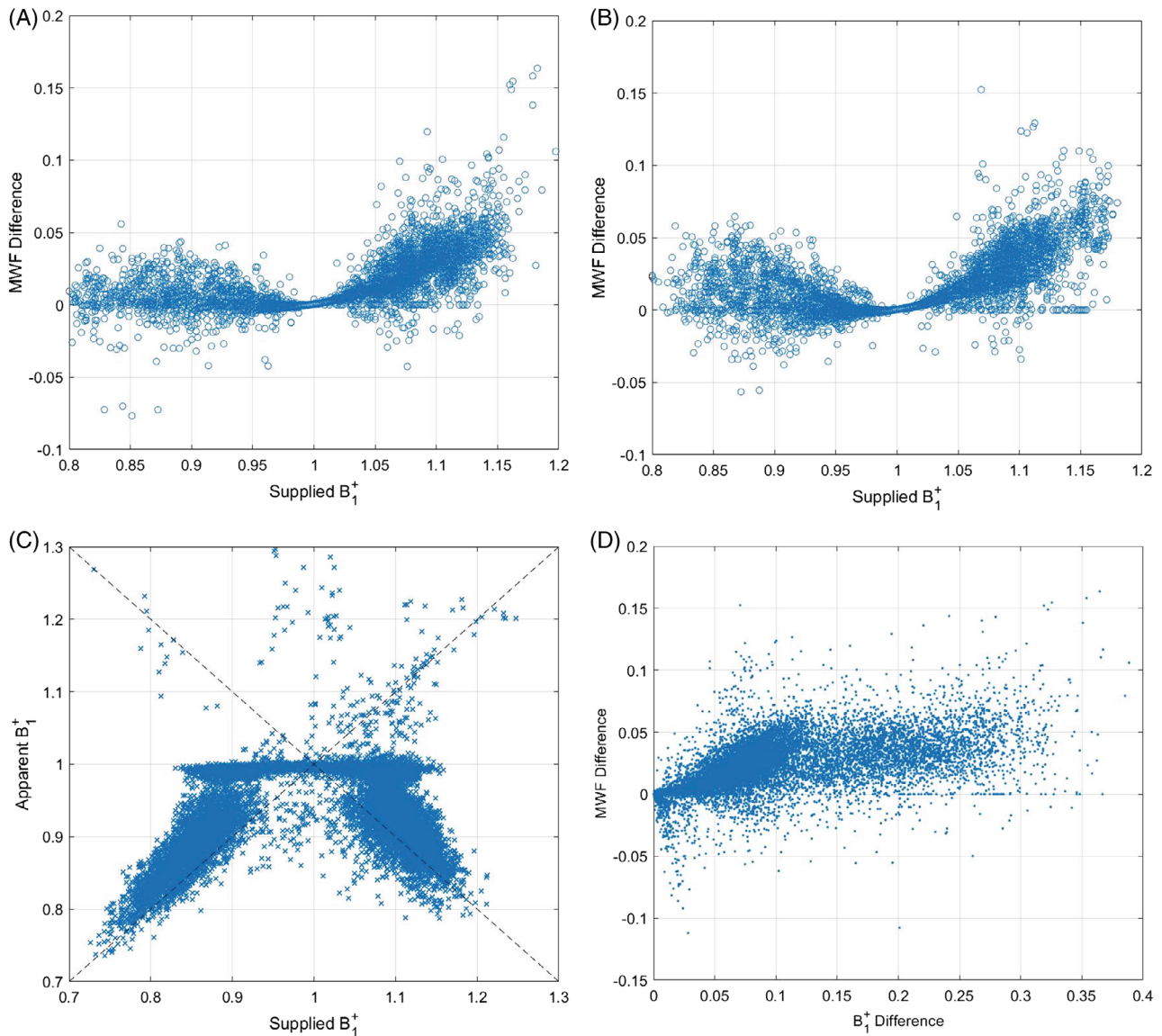


FIGURE 4 Scatter plots from in vivo experiments showing relationships between the MWF difference (supplied B_1^+ minus apparent B_1^+) and the B_1^+ values. (A,B) MWF difference versus the supplied B_1^+ values is shown for 2 subjects. Differences between methods increase when the supplied B_1^+ differs from 1.0, corresponding to 180° refocusing in these experiments. (C) Scatter plots of the apparent B_1^+ values versus supplied B_1^+ values from all subjects. (D) MWF difference versus the B_1^+ difference (supplied values minus the apparent values) from all subjects. In all cases, all voxels within white matter from 3 central slices were included

the proposed method (up to ~50% decrease depending on region).

Figure 4A,B shows in vivo scatter plots comparing supplied B_1^+ values and the MWF difference of the 2 methods for all WM voxels in central slices. Methods perform similarly at B_1^+ of 1.0 with larger MWF differences further from this value. Figure 4C shows the relationship between apparent B_1^+ and supplied B_1^+ for all subjects. Values near 1.0 tend to be estimated as 1.0, and generally, values under 1.0 get overestimated and values over 1.0 get severely underestimated. The relationship of MWF difference of the 2 methods compared to the difference of the B_1^+ values used in the fitting process is depicted in Figure 4D. The underestimation of apparent B_1^+ when the supplied B_1^+ is >1.0 , leads to underestimation of MWF, showing a similar pattern of negative bias in the MWF estimation as seen in Figure 2 for the special case of 15% MWF. The differences observed between the 2 figures are because of the constant value for MWF used in simulation, whereas in the in vivo experiments have a range of different MWF values contributing.

4 | DISCUSSION

The effects of B_1^+ error on MWF using regularized NNLS fitting were examined for 2D and 3D MESE and the feasibility of B_1^+ optimization supplied through an independent B_1^+ map was explored. Simulations showed biases in the optimization step can arise as SNR is reduced from ideal levels, especially in 2D MESE data where 2 distinct peaks appear in the B_1^+ histograms on opposing sides of $B_1^+ = 1.0$. The presence of the 2 peaks arises because of similar, but not exact decay curves around $B_1^+ = 1.0$ and the presence of noise might alter the estimation result to the wrong side, as previously seen in single component T_2 analysis.²⁶ The optimization step tries to acquire the smallest residual, over-fitting the noise (and artifacts) in the decay data. The scope of the B_1^+ misestimations in the apparent B_1^+ is more impactful for 2D MESE compared to 3D MESE. Increasing the relative refocusing to excitation width ratio improves 2D MESE results and large ratios, although impractical for multi-slice experiments, approach 3D MESE results.

For in vivo 2D MESE experiments, the use of the B_1^+ optimization step resulted in most central values in the apparent B_1^+ maps being near 1.0, which aligns with previous literature.²² The estimations were mostly <1.05 , which Akhondi-Asl et al²² used for the maximum value in their plots. When comparing the apparent B_1^+ map to the supplied B_1^+ map, large underestimations were observed where actual $B_1^+ > 1.05$, resulting in significant MWF underestimations.

MWF differences between using a supplied B_1^+ map and the apparent B_1^+ map from the standard decay train estimation have a strong spatial dependence on the B_1^+ pattern. MWF values across the entire WM, have a strong correlation ($0.98, P < 0.001$) between the 2 methods; however, local regions can differ substantially depending on B_1^+ misestimation errors. In particular, differences in the MWF estimations in areas with $B_1^+ > 1.05$ were ~ 0.04 , which is a large error considering the average MWF in WM was ~ 0.13 .

In a recent study by Lankford and Does,²³ constraining the flip angle was examined theoretically for single component T_2 fitting demonstrating analytically how bias in the flip angle estimation propagates to bias in T_2 estimates. In another study by Wiggermann et al,²¹ detailed examination of B_1^+ inhomogeneity and SNR was performed for multi-component myelin water calculations using 3D MESE (with nonselective refocusing). Our work extends from these works by examining MWF in 2D MESE sequences, while also including 3D MESE simulations for comparison. We found the value of an independent B_1^+ map was minimal for 3D MESE when SNR > 500 , which is in alignment with Wiggermann et al.²¹

For 2D MESE acquisitions, the slice profile gives rise to a range of flip angles across each voxel, therefore, either the Bloch equations need to be solved or EPG decay profiles need to be integrated across the slice.^{15,22,26} This increased complexity makes the results strongly affected by the B_1^+ field and without exact symmetry around $B_1^+ = 1.0$. Even for single component T_2 fitting of 2D MESE, which has only 3 unknowns per voxel, previous work has shown how B_1^+ misestimations from the decay curve may occur because of the lack of symmetry leading to T_2 errors that are improved by supplying a B_1^+ map.^{15,26} Previous work on 2D MESE multi-component T_2 analysis using Bloch,²² or EPG approaches,³³ showed plausible and reproducible results for MWF maps, but the effects of B_1^+ estimation were not examined thoroughly.

The 2D MESE sequences tend to have lower SNR levels than 3D (~ 300 in our experiments), which are under the sufficient values suggested for ideal MWI analysis (> 700),²⁸ therefore, a compromise on ideal SNR is needed for 2D MESE work, which then points to the value of an independent B_1^+ map. For 3D MESE methods, a higher SNR threshold is possible, but recent work with 3D GRASE has lower SNR (150-300 range).^{21,34,35} The high SNR requirement (700) for multi-component T_2 analysis of 3D MESE data is considered too strict in recent literature.^{21,27}

Prospective studies could include a rapid B_1^+ map, requiring only a small fraction of the time necessary for an MWI acquisition. Here, we used the Bloch-Siegert approach for supplying B_1^+ values, which, unlike the

double angle method, does not alter the excitation flip angle and uses an off-resonance pulse to induce a phase shift. The system SNR for our B_1^+ mapping sequence data was typically ~ 300 and at this SNR level the mapping method had higher accuracy and precision than the apparent B_1^+ measurement.³⁶ Although supplying a B_1^+ map is recommended particularly for 2D MESE, further improvements to B_1^+ estimation from the decay curve could add constraints on B_1^+ solutions, such as comparing results to a B_1^+ map template obtained from other studies on the same system. For example, recent work has shown only small B_1^+ variations across a large population using a single scanner.³⁷ Alternatively, deep learning methods can be used to create an adaptive model that estimates B_1^+ maps using multi-echo data.

A limitation of our work is the experimental validation was only for 2D MESE because of the lack of a 3D MESE sequence in our center. However, 3D MESE is an extremely slow approach, if methods such as compressed sensing are not used.³⁸ Many groups have recently used a 3D gradient and spin echo (GRASE) technique,^{10,19,20,38,39} although implementations vary between groups because of the complex nature of 3D GRASE. Nevertheless, our simulations show that 3D methods are much less affected by B_1^+ misestimations than 2D methods due both to the 2D flip angle effects that remove symmetry around 180° and typically reduced 2D SNR compared to 3D methods.

5 | CONCLUSION


For 2D MESE, because of increased complexity of decay curves and limited SNR, supplying B_1^+ improves MWF results in peripheral and central brain regions where flip angles differ substantially from 180° . This proposed approach alleviates further variability that miscalculation of B_1^+ may introduce to the NNLS solution.

ACKNOWLEDGMENTS

This work was supported by the Canadian Institutes of Health Research (MOP 102582); and the Natural Sciences and Engineering Research Council of Canada (RGPIN-2017-04006).

The code received from the UBC MRI Research Centre (<https://mriresearch.med.ubc.ca/news-projects/myelin-water-fraction/>) was the basis for development of 3D MESE simulation codes and MWF calculations.

ORCID

Nima Mehdizadeh  <https://orcid.org/0000-0003-3656-0029>

REFERENCES

- MacKay A, Whittall K, Adler J, Li D, Paty D, Graeb D. In vivo visualization of myelin water in brain by magnetic resonance. *Magn Reson Med*. 1994;31:673-677.
- Laule C, Kozlowski P, Leung E, Li DK, Mackay AL, Moore GR. Myelin water imaging of multiple sclerosis at 7 T: correlations with histopathology. *Neuroimage*. 2008;40:1575-1580.
- Laule C, Leung E, Lis DK, et al. Myelin water imaging in multiple sclerosis: quantitative correlations with histopathology. *Mult Scler*. 2006;12:747-753.
- MacKay A, Laule C, Vavasour I, Bjarnason T, Kolind S, Mädler B. Insights into brain microstructure from the T2 distribution. *Magn Reson Imaging*. 2006;24:515-525.
- Lee J, Hyun JW, Lee J, et al. So you want to image myelin using MRI: an overview and practical guide for myelin water imaging. *J Magn Reson Imaging*. 2021;53:360-373.
- Chen HS, Holmes N, Liu J, Tetzlaff W, Kozlowski P. Validating myelin water imaging with transmission electron microscopy in a rat spinal cord injury model. *Neuroimage*. 2017;153:122-130.
- Alonso-Ortiz E, Levesque IR, Pike GB. MRI-based myelin water imaging: a technical review. *Magn Reson Med*. 2015;73:70-81.
- Menon RS, Allen PS. Application of continuous relaxation time distributions to the fitting of data from model systems and excised tissue. *Magn Reson Med*. 1991;20:214-227.
- Jones CK, Xiang QS, Whittall KP, MacKay AL. Linear combination of multiecho data: short T2 component selection. *Magn Reson Med*. 2004;51:495-502.
- Wansapura JP, Holland SK, Dunn RS, Ball WS Jr. NMR relaxation times in the human brain at 3.0 tesla. *J Magn Reson Imaging*. 1999;9:531-538.
- Does MD. Inferring brain tissue composition and microstructure via MR relaxometry. *Neuroimage*. 2018;182:136-148.
- Möller HE, Bossoni L, Connor JR, et al. Iron, myelin, and the brain: neuroimaging meets neurobiology. *Trends Neurosci*. 2019;42:384-401.
- Birkel C, Birkel-Toeglhofer AM, Endmayr V, et al. The influence of brain iron on myelin water imaging. *Neuroimage*. 2019;199:545-552.
- Collins CM, Liu W, Schreiber W, Yang QX, Smith MB. Central brightening due to constructive interference with, without, and despite dielectric resonance. *J Magn Reson Imaging*. 2005;21:192-196.
- Lebel RM, Wilman AH. Transverse relaxometry with stimulated echo compensation. *Magn Reson Med*. 2010;64:1005-1014.
- Prasloski T, Mädler B, Xiang QS, MacKay A, Jones C. Applications of stimulated echo correction to multicomponent T2 analysis. *Magn Reson Med*. 2012;67:1803-1814.
- Jones C, Xiang Q, Whittall KP, MacKay A. Calculating T2 and B1 from decay curves collected with non-180_ refocusing pulses. In: Proceedings of the 11th Scientific Meeting, International Society for Magnetic Resonance in Medicine; 2003. p. 1018.
- Prasloski T, Rauscher A, MacKay AL, et al. Rapid whole cerebrum myelin water imaging using a 3D GRASE sequence. *Neuroimage*. 2012;63:533-539.
- Kumar D, Siemonsen S, Heesen C, Fiehler J, Sedlacik J. Noise robust spatially regularized myelin water fraction mapping with the intrinsic B1-error correction based on the linearized version of the extended phase graph model. *J Magn Reson Imaging*. 2016;43:800-817.

20. Drenthen GS, Backes WH, Aldenkamp AP, Op'tVeld GJ, Jansen JFA. A new analysis approach for T_2 relaxometry myelin water quantification: orthogonal matching pursuit. *Magn Reson Med*. 2019;81:3292-3303.
21. Wiggermann V, Vavasour IM, Kolind SH, MacKay AL, Helms G, Rauscher A. Non-negative least squares computation for in vivo myelin mapping using simulated multi-echo spin-echo T_2 decay data. *NMR Biomed*. 2020;33:e4277.
22. Akhondi-Asl A, Afacan O, Balasubramanian M, Mulkern RV, Warfield SK. Fast myelin water fraction estimation using 2D multislice CPMG. *Magn Reson Med*. 2016;76:1301-1313.
23. Lankford CL, Does MD. Propagation of error from parameter constraints in quantitative MRI: example application of multiple spin echo T_2 mapping. *Magn Reson Med*. 2018;79:673-682.
24. Hennig J. Multiecho imaging sequences with low refocusing flipangles. *J Magn Reson*. 1988;78:397-407.
25. Hennig J. Echoes—how to generate, recognize, use or avoid them in MR-imaging sequences. I. Fundamental and not so fundamental properties of spin echoes. *Concepts Magn Reson*. 1991;3:125-143.
26. McPhee KC, Wilman AH. Transverse relaxation and flip angle mapping: evaluation of simultaneous and independent methods using multiple spin echoes. *Magn Reson Med*. 2017;77:2057-2065.
27. Meyers SM, Laule C, Vavasour IM, et al. Reproducibility of myelin water fraction analysis: a comparison of region of interest and voxel-based analysis methods. *Magn Reson Imaging*. 2009;27:1096-1103.
28. Graham SJ, Stanchev PL, Bronskill MJ. Criteria for analysis of multicomponent tissue T_2 relaxation data. *Magn Reson Med*. 1996;35:370-378.
29. Chen L, Bernstein M, Huston J, Fain S. Measurements of T_1 relaxation times at 3.0 T: implications for clinical MRA. *Proceedings the 9th Annual Meeting of the International Society for Magnetic Resonance Medicine (Glasgow, Scotland)*. Vol 1. International Society for Magnetic Resonance in Medicine; 2001.
30. Labadie C, Lee JH, Rooney WD, et al. Myelin water mapping by spatially regularized longitudinal relaxographic imaging at high magnetic fields [published correction appears in *Magn Reson med*. 2015 Nov;74(5):1503]. *Magn Reson Med*. 2014;71:375-387.
31. Gudbjartsson H, Patz S. The Rician distribution of noisy MRI data [published correction appears in *Magn Reson med* 1996 Aug;36(2):332]. *Magn Reson Med*. 1995;34:910-914.
32. Weigel M. Extended phase graphs: dephasing, RF pulses, and echoes - pure and simple. *J Magn Reson Imaging*. 2015;41:266-295.
33. Drenthen GS, Backes WH, Aldenkamp AP, Jansen JFA. Applicability and reproducibility of 2D multi-slice GRASE myelin water fraction with varying acquisition acceleration. *Neuroimage*. 2019;195:333-339.
34. Wiggermann V, MacKay AL, Rauscher A, Helms G. In vivo investigation of the multi-exponential T_2 decay in human white matter at 7 T: implications for myelin water imaging at UHF. *NMR Biomed*. 2021;34:e4429.
35. Ljungberg E, Vavasour I, Tam R, et al. Rapid myelin water imaging in human cervical spinal cord. *Magn Reson Med*. 2017;78:1482-1487.
36. Park DJ, Bangerter NK, Javed A, Kaggie J, Khalighi MM, Morrell GR. A statistical analysis of the Bloch-Siegert B_1 mapping technique. *Phys Med Biol*. 2013;58:5673-5691.
37. MacLennan T, Seres P, Rickard J, Stolz E, Beaulieu C & Wilman AH. Characterization of B_1+ field variation at 3 tesla in 373 healthy brains over the lifespan. In *Proceedings of the 2021 ISMRM and SMRT Annual Meeting and Exhibition; May 9, 2021; No. 0501*.
38. Dvorak AV, Wiggermann V, Gilbert G, et al. Multi-spin echo T_2 relaxation imaging with compressed sensing (MET-RICS) for rapid myelin water imaging. *Magn Reson Med*. 2020;84:1264-1279.
39. Sacolick LI, Sun L, Vogel MW, Dixon WT, Hancu I. Fast radiofrequency flip angle calibration by Bloch-Siegert shift. *Magn Reson Med*. 2011;66:1333-1338.

How to cite this article: Mehdizadeh N, Wilman AH. Myelin water fraction mapping from multiple echo spin echoes and an independent B_1^+ map. *Magn Reson Med*. 2022;88:1380-1390. doi: 10.1002/mrm.29286